Planetary Spin and Obliquity from Mergers

Jiaru Li[1,2] and Dong Lai[1]

[1] Center for Astrophysics and Planetary Science, Department of Astronomy, Cornell University, Ithaca, NY 14853, USA; jiaru_li@astro.cornell.edu
[2] Theoretical Division, Los Alamos National Laboratory, Los Alamos, NM 87545, USA

Abstract

In planetary systems with sufficiently small inter-planet spacing, close encounters can lead to planetary collisions/mergers or ejections. We study the spin property of the merger products of two giant planets in a statistical manner using numerical simulations and analytical modeling. Planetary collisions lead to rapidly rotating objects and a broad range of obliquities. We find that, under typical conditions for two-planet scatterings, the distributions of spin magnitude S and obliquity θ_{SL} of the merger products have simple analytical forms: $f_S \propto S$ and $f_{\cos\theta_{\mathrm{SL}}} \propto (1 - \cos^2\theta_{\mathrm{SL}})^{-1/2}$. Through parameter studies, we determine the regime of validity for the analytical distributions of spin and obliquity. Since planetary mergers are a major outcome of planet–planet scatterings, observational search for the spin/obliquity signatures of exoplanets would provide important constraints on the dynamical history of planetary systems.

Unified Astronomy Thesaurus concepts: Exoplanet astronomy (486); Exoplanet dynamics (490); N-body simulations (1083)

1. Introduction

It has long been recognized that planet–planet interactions play an important role in shaping the architecture of planetary systems. Close planet encounters can lead to violent outcomes such as planetary mergers and ejections of one of the encountering planets.

There exists a great deal of literature on giant planet scatterings (e.g., Chambers et al. 1996; Rasio & Ford 1996; Lin & Ida 1997; Ford et al. 2001; Adams & Laughlin 2003; Chatterjee et al. 2008; Ford & Rasio 2008; Jurić & Tremaine 2008; Nagasawa & Ida 2011; Petrovich et al. 2014; Anderson et al. 2020). Most of these focus on ejections and using the remnants of scatterings to explain the eccentricity distribution of extrasolar giant planets.

In contrast, there has not been much discussion on the merger products. Numerical simulations indicate that the ratio of ejections to planet–planet collisions depends on the "Safronov number," the squared ratio of the escape velocity from the planetary surface to the planet's orbital velocity; when the Safronov number is less than unity, a significant fraction of planetary collisions are expected (e.g., Ford et al. 2001; Petrovich et al. 2014). A comprehensive study of scatterings in systems with three giant planets shows that the collision fraction increases from 50% at 1 au to more than 80% at 0.1 au (Anderson et al. 2020). Our recent study of two-planet scatterings, including hydrodynamical effects, shows that even at 10 au, the collision fraction can reach 40% (Li et al. 2020).

Previous studies on the collisions between protoplanetary objects have aimed mainly at understanding the process of late bombardment, during which collisions could be highly hyperbolic and the reaccretion efficiency is uncertain (Agnor & Asphaug 2004; Asphaug et al. 2006; Leinhardt & Stewart 2011; Stewart & Leinhardt 2012). However, for giant planet collisions resulting from orbital instabilities, the relative motions are close to parabolic (Anderson et al. 2020), and the planets merge without significant mass loss (Li et al. 2020; see also Leinhardt & Stewart 2011). This implies angular momentum conservation in the colliding "binary" planets for a wide range of impact parameters.

In this Letter, we study planetary spin and obliquity generated by giant planet collisions. It is well recognized that the spin of a planet (both magnitude and direction) may provide an important clue to its dynamical history. Various mechanisms have been suggested to produce nonzero planetary obliquities (e.g., Safronov & Zvjagina 1969; Benz et al. 1989; Korycansky et al. 1990; Tremaine 1991; Dones & Tremaine 1993; Lissauer et al. 1997; Hamilton & Ward 2004; Ward & Hamilton 2004; Morbidelli et al. 2012; Vokrouhlický & Nesvorný 2015; Millholland & Batygin 2019; Rogoszinski & Hamilton 2020; Su & Lai 2020). Despite the lack of direct measurement of extrasolar planetary spins and obliquities, constraints can be obtained using high-resolution spectroscopic observations (Snellen et al. 2014; Bryan et al. 2017, 2020). High-precision photometry of transiting planets can also help constrain planetary rotations in the future (e.g., Seager & Hui 2002; Barnes & Fortney 2003; Schwartz et al. 2016).

We carry out a suite of numerical experiments to determine the distributions of spin and obliquity of the planetary merger products. The simulations are designed similar to two giant planet scatterings experiments, but we focus on the results of collisions. Based on our recent work on the hydrodynamics of giant planet collisions (Li et al. 2020), we assume that two colliding planets always merge into a bigger one with no mass loss. The rest of this Letter is organized as follows. In Section 2, we present our fiducial numerical simulations and results. We then provide a simple analytical model in Section 3 to explain the numerical distributions of spin and obliquity. We examine the limitation of our analytical model using parameter studies in Section 4 and conclude in Section 5.

2. Fiducial Numerical Experiments

2.1. Setup of the Simulations and Assumptions

We consider a systems of two planets with masses $m_1 = 2M_{\mathrm{J}}$, $m_2 = 1M_{\mathrm{J}}$ and radii $R_1 = R_2 = R_{\mathrm{J}}$, orbiting a host star with mass $M_* = M_\odot$ and radius $R_\odot$. The initial spacing (in

semimajor axis) of the planets is given by

$$a_2 - a_1 = 2.5 R_{\rm H,mut}, \qquad (1)$$

where $R_{\rm H,mut}$ is the mutual Hill radius

$$R_{\rm H,mut} = \frac{a_2 + a_1}{2}\left(\frac{m_1 + m_2}{3 M_*}\right)^{1/3}. \qquad (2)$$

This spacing is smaller than the critical value ($2\sqrt{3}\,R_{\rm H,mut}$) for the Hill instability (Gladman 1993). In our fiducial runs, we use $a_1 = 1$ au. For each planet, we sample the initial eccentricity in the range [0.01, 0.05], the initial inclination in [$0°$, $2°$], and the argument of pericenter, longitude of ascending node, and mean anomaly in the range [0, 2π], assuming they all have uniform distributions.

The simulations are performed using the open-source N-body software package REBOUND[3] (Rein & Liu 2012). We choose the IAS15 integrator (Rein & Spiegel 2014) for high accuracy because the planets can have small separations. We run each simulation up to 10^5 initial orbital periods of the inner planet, and stop the simulation whenever one of the following conditions is reached:

1. Collision: the relative separation $|r_{\rm rel}|$ of the planets is equal to the sum of their physical radii (i.e., $|r_{\rm rel}| = R_1 + R_2$).
2. Ejection: one of the planets reaches a distance of 1000 au from the system's center of mass.
3. Star-grazing: the distance between the star and one of the planets is less than the solar radius.

We focus on collisions in this Letter. We assume the two planets have a perfect merger with no mass or angular momentum loss—this is justified by our hydrodynamical simulations (Li et al. 2020).

The initial (pre-merger) spin of each planet is unknown. The current 10 hr spin period of Jupiter and Saturn corresponds to 30% of the break-up rotation rate $\Omega_{\rm break} = (G M_{\rm p}/R_{\rm p}^3)^{1/2}$. Recent constraints on the spin of young planetary-mass companions also suggest that similar sub-break-up rotations are common for extrasolar giant planets (Bryan et al. 2017). Such a slow rotation rate may result from the magnetic disk braking during or immediately after the formation the planet (Takata & Stevenson 1996; Batygin 2018; Ginzburg & Chiang 2019). Adopting the moment of inertia $I \simeq 0.26 M_{\rm p} R_{\rm p}^2$ and initial spin $\Omega_i \sim 0.3\Omega_{\rm break}$, the initial spin angular momentum of each planet is $S_{\rm init} \sim 0.078 (G M_{\rm p}^3 R_{\rm p})^{1/2}$. On the other hand, the gravitational focusing between two giant planets can accelerate their relative speed to about $v_{\rm esc} = (2 G M_{\rm p}/R_{\rm p})^{1/2}$ just before their merger, introducing a relative orbital angular momentum of order of $M_{\rm p} R_{\rm p} v_{\rm esc} = (2 G M_{\rm p}^3 R_{\rm p})^{1/2}$, which is much larger than $S_{\rm init}$. Thus, we will assume the initial spin angular momentum of each planet is negligible in our analysis below.

With these assumptions, we can calculate the spin of the merger product as

$$S = \mu\, r_{\rm rel} \times v_{\rm rel}, \qquad (3)$$

where μ is the reduced mass of the two planets, $r_{\rm rel}$ and $v_{\rm rel}$ are the relative position and velocity between the planets at the moment of collision (see Figure 1). The maximum value of

---
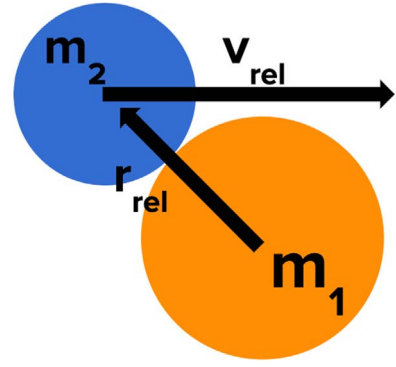
Figure 1. Geometry of the collision between two planets. $r_{\rm rel}$ and $v_{\rm rel}$ are the relative position and velocity of between the two planets, taking m_1 as the reference.
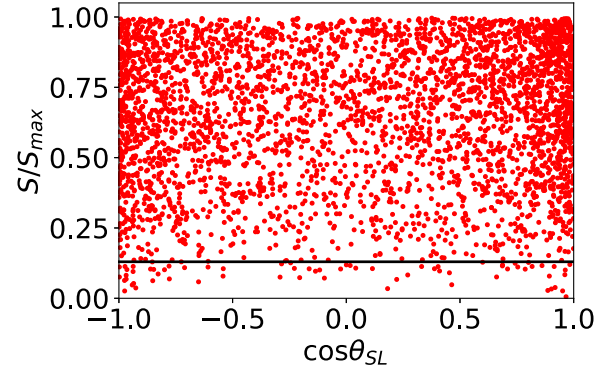
Figure 2. Spin and obliquity of the merger products found in our fiducial runs. The obliquity is displayed as $\cos\theta_{\rm SL}$ on the horizontal axis, and the spin is given in the unit of the maximum spin $S_{\rm max}$ (Equation (4)) on the vertical axis. The black line indicates the sum of the initial spins of the two planets (assuming each has $S_i = 0.3 I \Omega_{\rm break}$).

spin is reached when $r_{\rm rel}$ and $v_{\rm rel}$ are perpendicular to each other. Taking $|r_{\rm rel}| = R_1 + R_2$ and $|v_{\rm rel}|$ as the escape speed from $r_{\rm rel}$, we expect that

$$S_{\rm max} = \mu\sqrt{2 G (m_1 + m_2)(R_1 + R_2)} \qquad (4)$$

is the maximum value of the spin angular momentum generated by collisions.

Since the mutual inclination between the initial planetary orbits is small, the merged object has an orbital angular momentum closely aligned with the normal unit vector $\hat{n}$ of the initial zero-inclination plane. The planetary obliquity, $\theta_{\rm SL}$, is then given by

$$\cos\theta_{\rm SL} = \frac{\hat{n} \cdot S}{|S|}. \qquad (5)$$

2.2. Fiducial Results

Figure 2 shows the spin and obliquity of the merger products in our simulations. The values of spins are tightly bounded by the maximum given in Equation (4). Assuming both planets have an initial spin $0.3 I\Omega_{\rm break}$ (see Section 2.1), the total initial spin is less than $0.13 S_{\rm max}$. This means, in most cases, the relative orbital angular momentum at collision completely determines the final spin. Many merged objects have spins close to the maximum value, and they are strongly supported by rotation. Such an object may lose a significant amount of angular momentum through deaccretion and other processes,
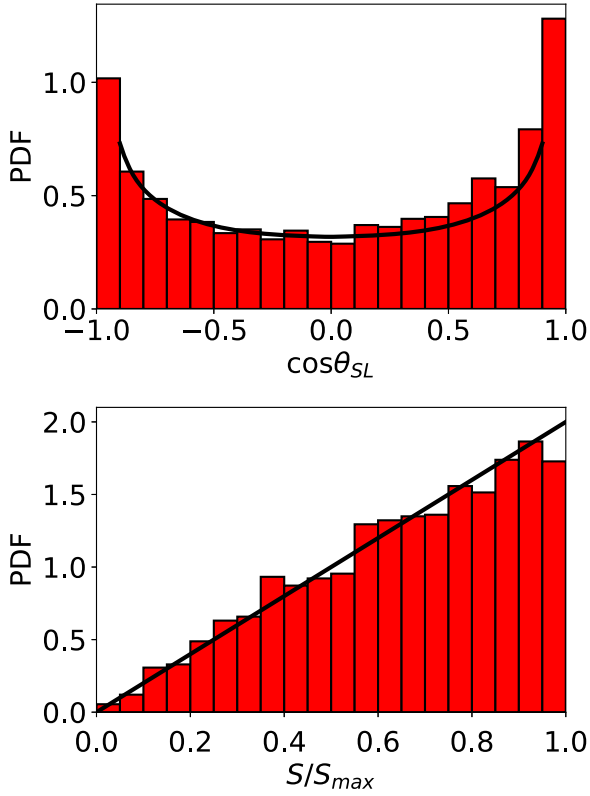
Figure 3. Obliquity (top) and spin (bottom) distribution of the merger products. The histograms are the numerical results found in our fiducial runs (with $a_1 = 1$ au, $m_1 = 2M_J$, $m_2 = 1M_J$, $R_1 = R_2 = R_J$, initial inclination i range $[0°, 2°]$). The black lines are the analytical distributions (Equations (13) and (14)) derived in Section 3.

but we expect no change of its obliquity in the absence of further strong interactions with other planets.

Figure 3 shows the marginalized distributions of obliquity and spin of the merged objects in our simulations. We also plot the analytical distributions derived in Section 3.

To gain some insight to the results, we investigate the geometry of collisions using Figure 4. The normal of the orbital plane is denoted by $\hat{n}$. For each collision event, we decompose $v_{\rm rel}$ into the vertical and "in-plane" components:

$$v_{\rm rel} = v_{\rm proj} + (v_{\rm rel} \cdot \hat{n})\hat{n} = |v_{\rm rel}|(\cos\theta_v \hat{v}_{\rm proj} + \sin\theta_v \hat{n}), \quad (6)$$

where $\hat{v}_{\rm proj} = v_{\rm proj}/|v_{\rm proj}|$. The top panel of Figure 4 indicates that, at the moment of collision, $v_{\rm rel}$ lies predominantly in the orbital plane. We define $\hat{\rho} = \hat{v}_{\rm proj} \times \hat{n}$ for each collision, and express $r_{\rm rel}$ as

$$r_{\rm rel} = |r_{\rm rel}|(\hat{n} \sin\theta_r \cos\phi_r + \hat{\rho} \sin\theta_r \sin\phi_r + \hat{v}_{\rm proj} \cos\theta_r), \quad (7)$$

where θ_r is the polar angle (with $\hat{v}_{\rm proj}$ pointing at the north pole) and ϕ_r is the azimuthal angle measured from $\hat{n}$. The middle panel of Figure 4 shows the distribution of ϕ_r. The bottom panel shows the distribution of θ_{rv} (the angle between $v_{\rm rel}$ and $r_{\rm rel}$) and θ_r (the angle between $v_{\rm proj}$ and $r_{\rm rel}$).

3. Analytic Model for the Spin and Obliquity Distributions

3.1. Analytical Distributions

Consider the moment when two planets collide (see Figure 1). We express $r_{\rm rel}$ as in Equation (7) and assume that the distribution of $\hat{r}_{\rm rel} = r_{\rm rel}/|r_{\rm rel}|$ is uniform inside a unit circle
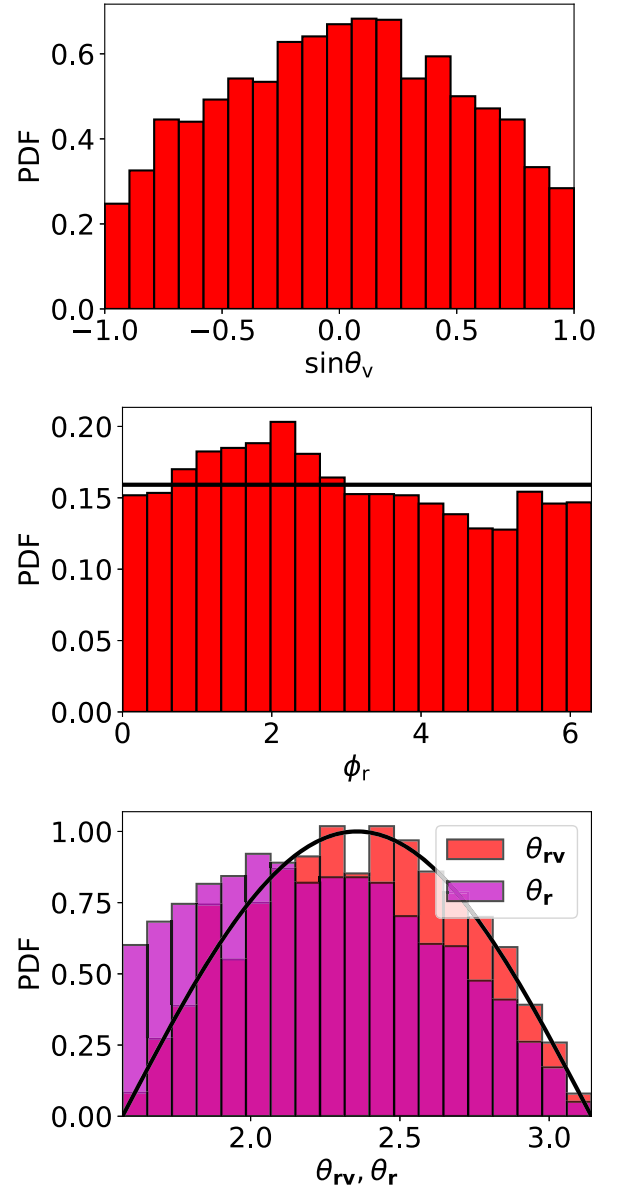
Figure 4. Distributions of θ_v (defined in Equation (6)), and ϕ_r and θ_r (defined in Equation (7)). The distribution of θ_{rv} (the angle between $v_{\rm rel}$ and $r_{\rm rel}$) is also shown for comparison. The histograms are the numerical results found in our fiducial runs, and the black lines are the analytical distributions (Equations (8) and (9)). Note that the θ_r histogram is shifted from Equation (8), but this does not affect the $\cos\theta_{\rm SL}$ and S distributions since the distribution of θ_{rv} agrees with Equation (8).

after being projected in the $\hat{n} - \hat{\rho}$ plane. Since the projection of $[\theta_r, \theta_r + d\theta_r] \times [\phi_r, \phi_r + d\phi_r]$ in the $\hat{n} - \hat{\rho}$ plane has an area of $\sin\theta_r d \sin\theta_r d\phi_r$, the distributions for θ_r and ϕ_r are

$$f_{\theta_r} = -2\sin\theta_r \cos\theta_r, \quad (8)$$

$$f_{\phi_r} = \frac{1}{2\pi}, \quad (9)$$

for θ_r from $\pi/2$ to π and ϕ_r from 0 to 2π. The two distributions are plotted as black lines in Figure 4. We find an excellent matching between the analytical curves and the numerical results, except for a small asymmetry in the numerical ϕ_r distribution and a shift in the θ_r distribution. This asymmetry implies a preferential alignment between the spin and the

orbital angular momentum of the merger product over anti-alignment. The shift is due to the nonzero values of θ_ν.

We further assume that the planets have a sufficiently low mutual inclination so that $\boldsymbol{v}_{\rm rel} \simeq \boldsymbol{v}_{\rm proj}$ (see the top panel of Figure 4). From Equations (3)–(4), the spin of the merger product can be written as

$$S = S_{\max}(\hat{\boldsymbol{n}} \sin\theta_{\boldsymbol{r}} \sin\phi_{\boldsymbol{r}} - \hat{\boldsymbol{\rho}} \sin\theta_{\boldsymbol{r}} \cos\phi_{\boldsymbol{r}}). \tag{10}$$

Thus, the spin magnitude and the obliquity are

$$S/S_{\max} = \sin\theta_{\boldsymbol{r}}, \tag{11}$$

$$\cos\theta_{\rm SL} = \sin\phi_{\boldsymbol{r}}. \tag{12}$$

The distribution of $S/S_{\max}$ is then given by

$$f_{S/S_{\max}} = f_{\theta_{\boldsymbol{r}}} \left| \frac{d(S/S_{\max})}{d\theta_{\boldsymbol{r}}} \right|^{-1} = 2\sin\theta_{\boldsymbol{r}} = 2\frac{S}{S_{\max}}. \tag{13}$$

The distribution of $\cos\theta_{\rm SL}$ is

$$f_{\cos\theta_{\rm SL}} = 2f_{\phi_{\boldsymbol{r}}} \left| \frac{d\cos\theta_{\rm SL}}{d\phi_{\boldsymbol{r}}} \right|^{-1} = \frac{1}{\pi|\cos\phi_{\boldsymbol{r}}|}$$

$$= \frac{1}{\pi} \frac{1}{\sqrt{1 - \cos^2\theta_{\rm SL}}}, \tag{14}$$

where the factor of 2 comes from the fact that the inverse function of $\sin\phi_{\boldsymbol{r}}$ is double valued for $\phi_{\boldsymbol{r}}$ from 0 to 2π. The two analytical distributions are plotted as black lines in Figure 3, showing excellent agreement to the numerical results.

3.2. Validity and Limitation

There are mainly two limitations to our analytical distributions. The first occurs when the initial mutual inclination between the planetary orbits is too small. Our assumption of the $(\theta_{\boldsymbol{r}}, \phi_{\boldsymbol{r}})$ distribution (Equations (8) and (9)) requires equal accessibility to any points in the area perpendicular to $-\hat{\boldsymbol{v}}_{\rm proj}$. This is possible only when the initial mutual inclination between the two planetary orbits is at least a few times larger than $R_{\rm p}/a_1$.

The second limitation occurs when the initial mutual inclination is too large. In Section 3.1 we have assumed $|\boldsymbol{v}_{\rm rel} \cdot \hat{\boldsymbol{n}}| \ll |\boldsymbol{v}_{\rm proj}|$, or $\theta_\nu \simeq 0$. Suppose the outer planet (initially at semimajor axis a_2) moves to the inner planet (at a_1) and enters the mutual Hill sphere. At this point, their relative velocity in orbital plane can be estimated as $v_\parallel \sim \sqrt{GM_*a_2}/a_1 - \sqrt{GM_*/a_1} \simeq (\Delta a/2a_1)\sqrt{GM_*/a_1}$, where $\Delta a = a_2 - a_1$. On the other hand, the vertical velocity difference almost solely comes from the mutual inclination, $v_\perp \sim \sqrt{GM_*/a_1} \sin i$. After entering the mutual Hill sphere, the relative motion between the two planets is governed by their mutual gravitational attraction, and the orientation of the "binary" relative to the original orbital plane remains approximately constant. Thus, at collision, the inclination angle (θ_ν) of $\boldsymbol{v}_{\rm rel}$ relative to the original orbital plane is given by $\tan\theta_\nu \sim (2a_1/\Delta a)\sin i$. The condition $\theta_\nu \ll 1$ is equivalent to $\sin i \ll \Delta a/(2a_1)$.

When θ_ν is nonnegligible, we expect that, instead of the $\hat{\boldsymbol{n}}$–$\hat{\boldsymbol{\rho}}$-plane, $\hat{\boldsymbol{r}}_{\rm rel}$ is uniform in the plane normal to the actual relative velocity $\boldsymbol{v}_{\rm rel}$. The distribution of $|\boldsymbol{S}|$ would be similar to that derived in Section 3.1 (since the change from $\hat{\boldsymbol{v}}_{\rm proj}$ to $\hat{\boldsymbol{v}}_{\rm rel}$ amounts to a simple rotation of the coordinate system).

However, the obliquity becomes

$$\cos\theta_{\rm SL} = \cos\theta_\nu \sin\theta_{\boldsymbol{r}} \sin\phi_{\boldsymbol{r}}/|\boldsymbol{S}|. \tag{15}$$

A finite θ_ν tends to reduce $|\cos\theta_{\rm SL}|$, with the corresponding change in the distribution of $\cos\theta_{\rm SL}$.

In summary, we expect that the analytical distribution of $\theta_{\rm SL}$ (Equation (14)) to be valid when

$$\frac{R_{\rm p}}{a_1} \ll \sin i \ll \frac{\Delta a}{2a_1} \simeq \frac{K}{2}\left(\frac{m_1 + m_2}{3M_*}\right)^{1/3}, \tag{16}$$

where we have used $\Delta a = K R_{\rm H,mut}$ (see Equation (2)). On the other hand, the analytical distribution of S (Equation (13)) is valid when

$$\frac{R_{\rm p}}{a_1} \ll \sin i. \tag{17}$$

For the fiducial numerical simulations presented in Section 2, these conditions are well satisfied: an initial inclination of $2°$ corresponds to $73R_{\rm J}/(1\ {\rm au}) = 0.035$, and is much less than $\Delta a/(2a_1) = 0.14$. So it is not surprising that $S/S_{\max}$ and $\theta_{\rm SL}$ follow the analytical distributions very well.

4. Parameter Studies

We perform parameter studies by carrying out simulations with different initial semimajor axis, mutual inclination, and planet radius to test the validity and limitations of our fiducial results (Section 2) and analytical formulae (Section 3).

4.1. Initial Semimajor Axis

Note that varying a_1 also changes a_2 according to Equation (1). Increasing a_1 makes ejections more likely than collisions as the outcomes of planetary scatterings show (see Li et al. 2020). It also makes the systems safer from the lower limit in Equations (16)–(17). As expected, the top row of Figure 5 shows that the distributions of the spin and obliquity for different a_1 values are the same as the fiducial results.

4.2. Initial Inclination

We investigate the effect of the initial inclination by changing the upper limit of the initial inclination, $2°$, to different values of $i_{\max}$.

The second row of Figure 5 shows the results for small $i_{\max}$. Note that $i_{\max} = 0°.1$ and $2°.0$ correspond to 3.7 and $73(R_{\rm J}/a_1)$, respectively. For small $i_{\max}$, we expect the analytical distributions $f_{\theta_{\boldsymbol{r}}}$ and $f_{\phi_{\boldsymbol{r}}}$ (Equations (8) and (9)) to fail (see Equations (16) and (17)). The numerical result shows that obliquities are more concentrated around $0°$ or $180°$ for $i_{\max} = 0°.1$ and $0°.3$, and the distribution of the spin magnitude tends to be more uniform.

The third row of Figure 5 shows the results for $i_{\max}$ equal to a few degrees. In this range, the simulated systems are safe from the lower inclination limit of Equations (16)–(17). As expected (Section 3.2), the analytical distribution for $S/S_{\max}$ matches the numerical results well. However, as $i_{\max}$ increases to more than $4°$, the numerical obliquity distribution starts to deviate from the analytical expression. Using $\tan\theta_\nu \sim (2a_1/\Delta a)\sin i$, we find that $\tan\theta_\nu \sim 0.24$, 0.49, and 0.73 for $i = 2°$, $4°$, and $6°$, respectively. Hence, for $i_{\max} = 4°$ and $6°$, our analytic $\cos\theta_{\rm SL}$ distribution becomes inaccurate.
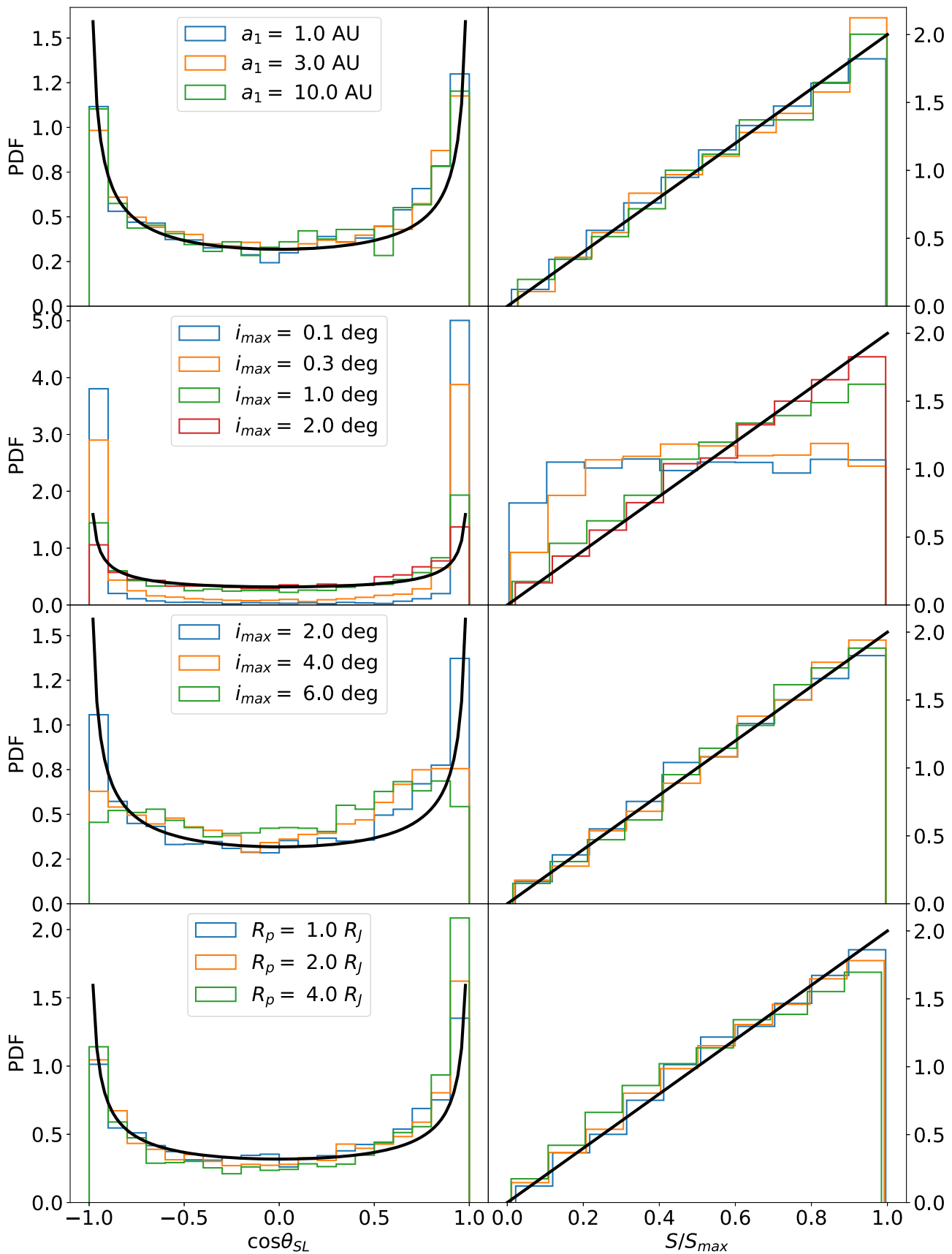
Figure 5. Same as Figure 3, except for different values of the parameter used in the simulations. Top row: initial a_1; middle two rows: i_{max} (the initial inclinations of both planets are sampled from $[0, i_{max}]$); bottom row: the planet radius R_p as labeled.

4.3. Size of Planet

Varying the size of the planets can change the branching ratio of mergers versus ejections (see Li et al. 2020), but does not cause any change to our results concerning the spin and obliquity distributions, as long as the condition $R_p/a_1 \ll i_{max}$ is satisfied. Note that the value of R_p is irrelevant to our assumption of $\theta_v \simeq 0$ (i.e., $\boldsymbol{v}_{rel}$ is in the orbital plane). The bottom row of Figure 5 shows the results. The magnitude of the spin is normalized by different S_{max} according to the planet's radius. As expected, the plots are similar to the fiducial results (Figure 3).

5. Summary and Discussion

We have carried out a suite of numerical simulations of the dynamical evolution of two giant planets, initially in quasi-circular unstable orbits, to determine the distributions of spin and obliquity of the planet merger products. While many previous works have studied giant planet scatterings, our work is the first (as far was we know) to systematically determine the spin property of the planet mergers. Based on our recent work on the hydrodynamics of giant planet collisions (Li et al. 2020), we assume that two colliding planets always merge into a bigger one with no mass or angular momentum losses. For reasonable initial (pre-merger) rotations of the planets, the spin angular momentum of the merger product is dominated by the relative orbital angular momentum of the colliding planets at contact.

Our most important finding is displayed in Figure 3, showing the distributions of $\cos\theta_{SL}$ (where θ_{SL} is the obliquity or spin–orbit misalignment angle) and spin S (in units of the maximum possible value) of the planet merger products in our fiducial runs. We develop a simple model and show that these distributions are well described by the analytical expressions (Equations (13) and (14))

$$f_{S/S_{max}} = 2S/S_{max}, \quad f_{\cos\theta_{SL}} = \frac{1}{\pi\sqrt{1 - \cos^2\theta_{SL}}}. \quad (18)$$

In addition, we carry out parameter studies to explore the validity of these distributions under various conditions (Section 4). The key is the initial mutual inclination Δi of the planetary orbits, which is limited by i_{max} in our parameter studies, in relation to the size R_p and initial spacing Δa of the planets (see Equations (16) and (17)). We find that the analytic distribution of S works well as long as Δi is much greater than R_p/a (Equation (17)), while the analytic distribution of $\cos\theta_{SL}$ further requires that Δi be much less than $\Delta a/(2a)$ (Equation (16))—when this condition is not satisfied, a more uniform distribution of $\cos\theta_{SL}$ is obtained (see the third row of Figure 5).

A possible caveat of this study is that we have neglected tidal effects in close planet–planet encounters. Numerical simulations of planet scatterings including hydrodynamical effects show that the main change is the collision versus the ejection branching ratio. The obliquity distribution is largely unchanged, while the $f_{S/S_{max}} \propto S$ up to $S \simeq 0.8S_{max}$ because of the tidal effects. (Li et al. 2020).

While in this Letter we have focused on mergers of giant planets, we expect that similar results may hold for mergers of smaller planets such as super-Earths and mini-Neptunes. We simply need to compare Δi, R_p/a and $\Delta a/(2a)$ to determine the regimes of validity of our analytical and numerical results.

Overall, our study shows that planetary mergers predominantly produce rapidly rotating objects. These objects are rotationally supported, and are obviously quite different from the "usual" planets. Their spins may undergo further evolution, so the present-day distribution of S could be different from what is predicted in this Letter. However, we expect the obliquity and its distribution to be more long-lasting when there is no strong external perturbation. Observational searches for the merger signatures in the form of spin and obliquity, for various types of planets, will be valuable in constraining the dynamical history of planetary systems.

ORCID iDs

Jiaru Li ⬤ https://orcid.org/0000-0001-5550-7421
Dong Lai ⬤ https://orcid.org/0000-0002-1934-6250

References

Adams, F. C., & Laughlin, G. 2003, Icar, 163, 290
Agnor, C., & Asphaug, E. 2004, ApJL, 613, L157
Anderson, K. R., Lai, D., & Pu, B. 2020, MNRAS, 491, 1369
Asphaug, E., Agnor, C. B., & Williams, Q. 2006, Natur, 439, 155
Barnes, J. W., & Fortney, J. J. 2003, ApJ, 588, 545
Batygin, K. 2018, AJ, 155, 178
Benz, W., Slattery, W. L., & Cameron, A. G. W. 1989, Metic, 24, 251
Bryan, M. L., Benneke, B., Knutson, H. A., Batygin, K., & Bowler, B. P. 2017, NatAs, 2, 138
Bryan, M. L., Chiang, E., Bowler, B. P., et al. 2020, AJ, 159, 181
Chambers, J., Wetherill, G., & Boss, A. 1996, Icar, 119, 261
Chatterjee, S., Ford, E. B., Matsumura, S., & Rasio, F. A. 2008, ApJ, 686, 580
Dones, L., & Tremaine, S. 1993, Icar, 103, 67
Ford, E. B., Havlickova, M., & Rasio, F. A. 2001, Icar, 150, 303
Ford, E. B., & Rasio, F. A. 2008, ApJ, 686, 621
Ginzburg, S., & Chiang, E. 2019, MNRAS, 491, L34
Gladman, B. 1993, Icar, 106, 247
Hamilton, D. P., & Ward, W. R. 2004, AJ, 128, 2510
Hunter, J. D. 2007, CSE, 9, 90
Jurić, M., & Tremaine, S. 2008, ApJ, 686, 603
Korycansky, D., Bodenheimer, P., Cassen, P., & Pollack, J. 1990, Icar, 84, 528
Leinhardt, Z. M., & Stewart, S. T. 2011, ApJ, 745, 79
Li, J., Lai, D., Anderson, K. R., & Pu, B. 2020, arXiv:2006.10067
Lin, D. N. C., & Ida, S. 1997, ApJ, 477, 781
Lissauer, J. J., Berman, A. F., Greenzweig, Y., & Kary, D. M. 1997, Icar, 127, 65
Millholland, S., & Batygin, K. 2019, ApJ, 876, 119
Morbidelli, A., Tsiganis, K., Batygin, K., Crida, A., & Gomes, R. 2012, Icar, 219, 737
Nagasawa, M., & Ida, S. 2011, ApJ, 742, 72
Petrovich, C., Tremaine, S., & Rafikov, R. 2014, ApJ, 786, 101
Rasio, F. A., & Ford, E. B. 1996, Sci, 274, 954
Rein, H., & Liu, S.-F. 2012, A&A, 537, A128
Rein, H., & Spiegel, D. S. 2014, MNRAS, 446, 1424
Rogoszinski, Z., & Hamilton, D. P. 2020, ApJ, 888, 60
Safronov, V., & Zvjagina, E. 1969, Icar, 10, 109
Schwartz, J. C., Sekowski, C., Haggard, H. M., Pallé, E., & Cowan, N. B. 2016, MNRAS, 457, 926
Seager, S., & Hui, L. 2002, ApJ, 574, 1004
Snellen, I. A. G., Brandl, B. R., de Kok, R. J., et al. 2014, Natur, 509, 63
Stewart, S. T., & Leinhardt, Z. M. 2012, ApJ, 751, 32

Su, Y., & Lai, D. 2020, arXiv:2004.14380
Takata, T., & Stevenson, D. J. 1996, Icar, 123, 404
Tremaine, S. 1991, Icar, 89, 85

van der Walt, S., Colbert, S. C., & Varoquaux, G. 2011, CSE, 13, 22
Vokrouhlický, D., & Nesvorný, D. 2015, ApJ, 806, 143
Ward, W. R., & Hamilton, D. P. 2004, AJ, 128, 2501